CHAPTER 4

PIC Simulation and Results

4.1 Introduction

Simulation tools play an essential role in research and development. Properly calibrated simulation tools can predict device behavior with high accuracy. Hence, the resources and time involved in actual prototyping and testing can be reduced to a great extent. Simulation tools like; Poisson SUPERFISH,[*] 1D trajectory code, 2D PIC code ISIS, and 3D PIC code MAGIC have been used to design and improve reltron's performance during the early developments. Still, there is ample scope of advanced simulation tools for better understanding the device operation and exploring its prospects.

This chapter covers; the arrangement of a PIC simulation setup that includes probes and monitors for recording the outputs, and presents the result and adjoining discussions.

4.2 PIC Solver of CST MWS

The PIC solver is appropriate for studying the non-linear interaction between particles and field in vacuum electronics devices like klystron, magnetron, travelling wave tube, etc. Here, finite integration technique (FIT) [Weiland *et al.* (1977)] based CST PARTI-

---

[*] for calculating static and RF fields in 2D Cartesian coordinates or axially symmetric cylindrical coordinates. This freely available code was developed by the Los Alamos Accelerator Code Group.

CLE STUDIO^{TM} [CST Studio Suite (2020)] has been used. This solver combines non-orthogonal co-ordinate system with the Cartesian system, and divides the problem space into into finite numbers of tetrahedral or hexahedral cells by dual grid type discretization technique [Clemens *et al.*(2001)]. Each cell fits exactly with each other forming – point, linear and planar intersection regions that serve as primal computational grids. Voltages are assigned to these primal grids at the edges and magnetic flux are assigned through the facets. The primal grid and its dual (incorporating the electric flux and currents) completely discretize the integral form of all four Maxwell's equations in any type of time dependent behavior [Balk (2008)]. This dual grid type of discretization uses Crank-Nicolson scheme [Sun *et al.* (2003)] along with other mathematical formulas to calculate stability and energy conservation before starting with numerical calculations. The particle trajectory is estimated by considering the relativistic factor (if any) and the available electric and magnetic fields that exert Lorentz force on the particle in combination with eigenmode fields. This self-consistent solver tracks the particles in continuous phase space by computing fields at those discrete locations. Linear interpolation scheme is used for computing the particle current from the fields and vice-versa. The minimum mesh step in the discretization determines the maximum usable time step. The method persists stability as long as the time step for the integration remains less than a specified limit. So, a denser grid supports a smaller step width. Hence, this solver requires intensive computational resources. The graphics processing unit (GPU) acceleration option can be used to improve the performance and minimize the simulation time required by the PIC solver.

4.3 Modeling and Simulation Set-up

A detailed description of the simulation set-up that replicates the experimental procedure is given below.

Modulation section: An S-band reltron tube is designed according to the design methodology [Miller *et al.* (1992), (1994)], [Mahto et al. (2016)], and modeled (Figure 4.1) in CST MWS for studying the effect of electron beam and the associated space charge wave propagation. The dimensions and materials used in the simulation are listed in Table 4.1.

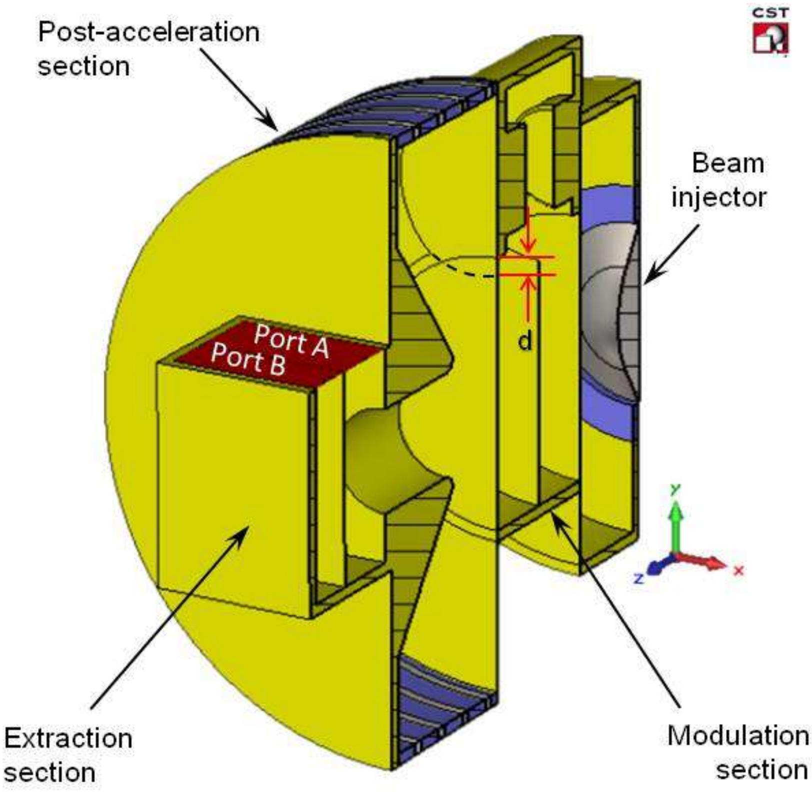

Figure 4.1: Cross sectional view of S-band reltron showing different sections, and the coupling depth (d).

Driving supply: The pulsed power supply drives the cathode as well as the postacceleration section of reltron. To simulate the effect of PFN Marx generator with resistive divider and crowbar switch, which is suitable for an S-band reltron, a rectangular pulse with a rise time of 10 nS has been defined as a new input signal, and used for driving two sets of discrete voltage ports. Each sets are made symmetric about the beam axis and assigned with the desired cathode and postacceleration potentials. This serves the purpose of the resistive voltage divider. The input signal gets automatically terminated after the preset pulse duration, like the crowbar switch that terminates the voltage pulse.

Cathode: Dielectric velvet cathodes [Miller (1998)] were used in the original work for their associated advantages like low electric field threshold, high current density, low plasma closure velocity, and cost effectiveness [Miller *et al.* (1998)]. Here we have used the explosive emission model on a stainless steel cathode and got nearly the same device performance. In explosive emission, a space charge limited current is emitted by a cold cathode resulting from a high, user-specified electric field. Hence, the current is not an input parameter. As the beam traverses the gridded end walls of the modulation section, the associated space charge wave interact with all the cavity modes. Only $\pi/2$ mode grows by gaining energy from the beam and eventually acts as a 'gate,' alternately stopping and accelerating the beam that results in dense electron bunches [Miller *et al.* (1992)].

Postacceleration section: A high positive potential boosts the kinetic energy of all the electrons in the bunched beam at the exit of the modulation section. A set of discrete ports are driven by an input signal to create the effect of postacceleration section.

Output extraction section: The extraction section is modeled by terminating a standard WR284 waveguide at one end (along xz plane) and divided it into two cavities with a grid (along xy plane) as shown in Figure 4.1. The length of the waveguide is optimized parametrically for maximum amplitude of the port signals.

Table 4.1: Dimensions and Materials Used in PIC Simulation

List of parameters / materials / dimensions	Values
Cathode potential	200 kV
Post acceleration potential	400 kV
Rise time of input signal	10 nS
Grid transparency	90 %
Cathode material	Stainless steel
Cavity and grid material	Cu (σ = 5.8 × 10^8 S/m)
Insulator material	Plexiglas (σ = 0.02 S/m)
Main cavity length (l_mc)	42.5 mm
Main cavity radius (r_mc)	36.8 mm
Side cavity length (l_sc)	34 mm
Side cavity radius (r_sc)	25.8 mm
Idler disc length (l_idl)	11 mm
Idler disc radius (r_idl)	13.75 mm
Anode cathode gap	17 mm
Post acceleration gap	51.25 mm
Extraction section	WR284 (72.14×34.04 mm)

4.4 Results and Discussions

Two simulations have been carried out to study the effect of i) coupling depth (d), and ii) idler disc length (l_idl) on reltron's performance. The results are presented and interpreted in the following subsections.

4.4.1 Temporal port-signal and output power

The RF signal resulting from the beam field interaction is recorded by the port signal. Two waveguide ports are assigned at each of the cavity opening (port A and B in Figure 4.1) for recording the time-varying RF signals as shown in Figure 4.2. In the original work [Miller *et al.* (1992)], the output was radiated by a horn antenna and measured by a calibrated B-dot probe in anechoic chamber. An alternate way was also reported, which is measuring the power from a calibrated directional coupler. The temporal port signal produced by the simulation has the dimension of $\sqrt{W}$ [CST Studio Suite (2020)]. So, the resultant output power (W) at various coupling depths is shown in Figure 4.3.

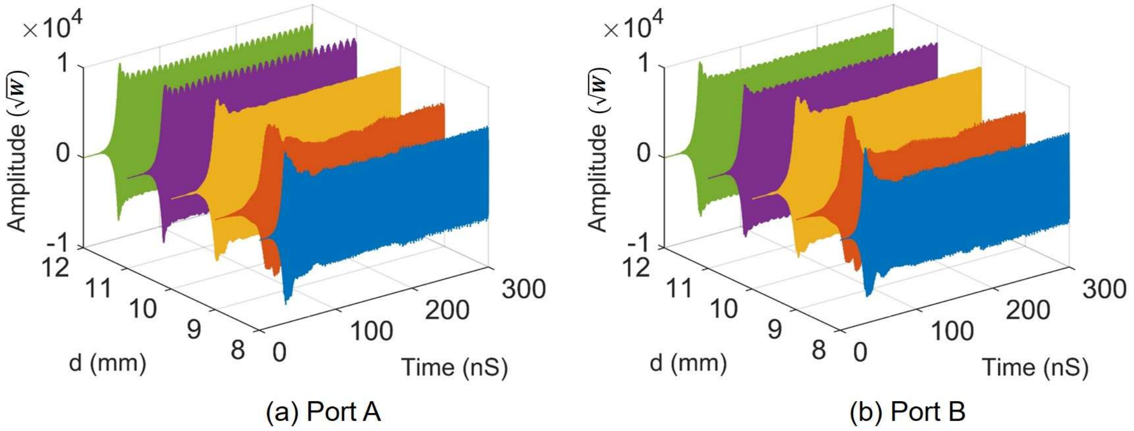

(a) Port A

(b) Port B

Figure 4.2: Temporal signals from the waveguide ports for different coupling depth (d).

4.4.2 Oscillation frequency

The oscillation frequency can be obtained by Fourier transform (FT) of the port signal in the post-processing window. The FT of signal from port A at different values of d is

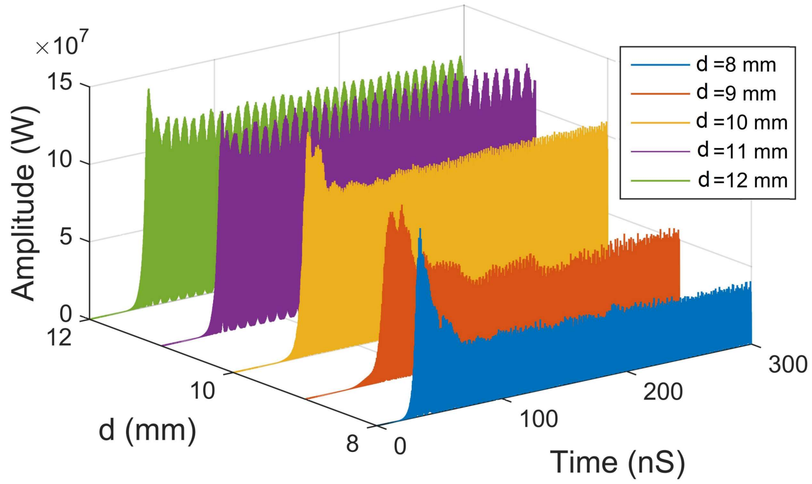

Figure 4.3: Total output power for different coupling depth (d).

shown in Figure 4.4. From the spectrum, it is observed that the oscillation frequency is closest to the cold frequency of $\pi/2$ mode. This confirms that $\pi/2$ mode is responsible for the beam bunching. The frequency has reduced by a few tens of MHz than the cold frequency due to beam loading. The purity of the respective oscillation frequencies can be observed from the narrow spectral width shown in figure inset. Figure 4.4 also shows a gradual decrease in oscillation frequency with increasing d. This is due to the decline in the $\pi/2$ mode frequency, resulting from increased k with d, as shown in Figure 3.5 in Chapter 3. Traces of higher-order harmonics of the fundamental mode are also found in the spectrum.

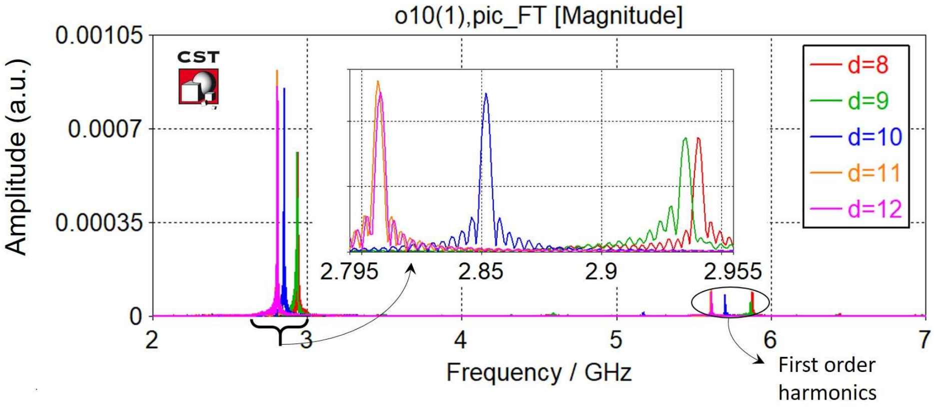

Figure 4.4: The spectrum of port signal for different coupling depth (d), showing the fundamental modes and their harmonics. An enlarged view of the fundamental mode is shown inset.

4.4.3 Temporal current signals

In the experimental works [Miller *et al.* (1992)], the beam current was measured using Rogowski coil at the entrance of extraction section. In simulation, the currents are recorded by current monitors at different sections of the tube. Circular loops are modeled and translated to the respective positions, and current monitors are defined from the loops. It was ensured that each current monitor completely encloses the plane through which the electron beam passes. The temporal current signals at the anode-cathode (AK) gap, middle of the first and the second cavity, and at the extraction section is shown in Figure 4.5.

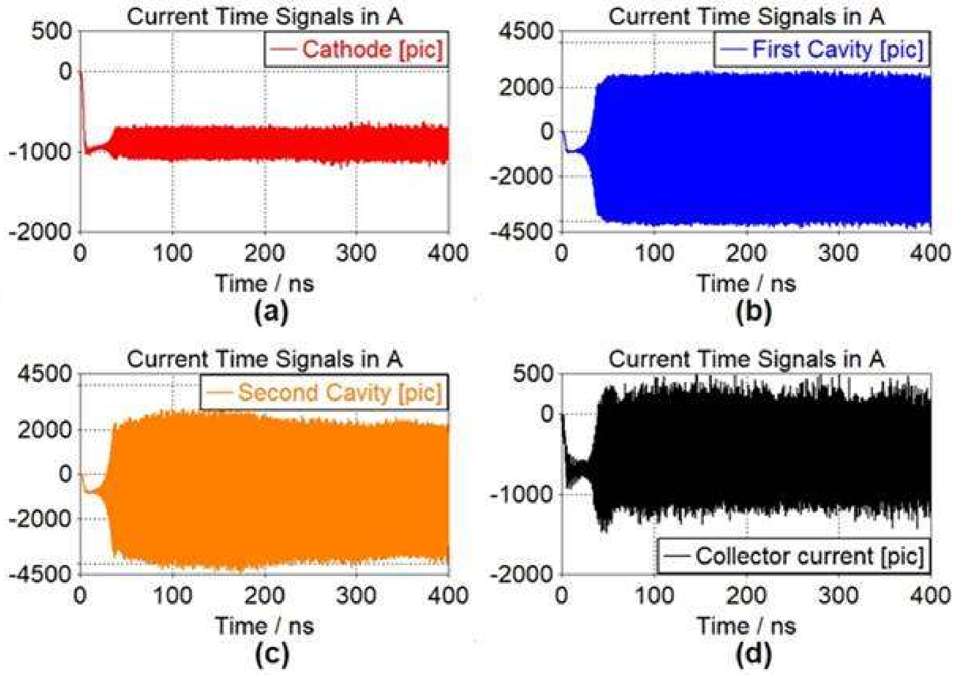

Figure 4.5: Temporal currents at (a) cathode, (b) first cavity, (c) second cavity, and (d) collector.

A larger variation in temporal current amplitude indicates higher difference of electron density in the bunched beam, and hence, higher beam current modulation. The beam modulation is the highest in the first and the second cavity of the modulation section, as shown in Figure 4.5 (b), and (c). The current in the AK-gap varies by a relatively small amplitude due to this intense beam modulation (Figure 4.5 (a)). The beam modulation decreases significantly in the spent beam (Figure 4.5 (d)) as the beam kinetic energy is transferred to the RF field in the extraction section.

4.4.4 Frequency tunability

Retron's operating frequency can be tuned with ease by changing various dimensional parameters of the modulation section. Miller *et al.* have reported mechanical tuning by varying the main cavity radius (r_mc) through single sides and double sided tuning plungers [Miller *et al.* (1998)]. Here, the device tunability has been studied by changing three dimensional parameters through parametric sweeps, the main cavity radius (r_mc), the idler disc length (l_idl), and the coupling depth (d). The interval plot in Figure 4.6 shows the frequency tunability achievable through modifying these cavity parameters, and the corresponding cold frequencies.

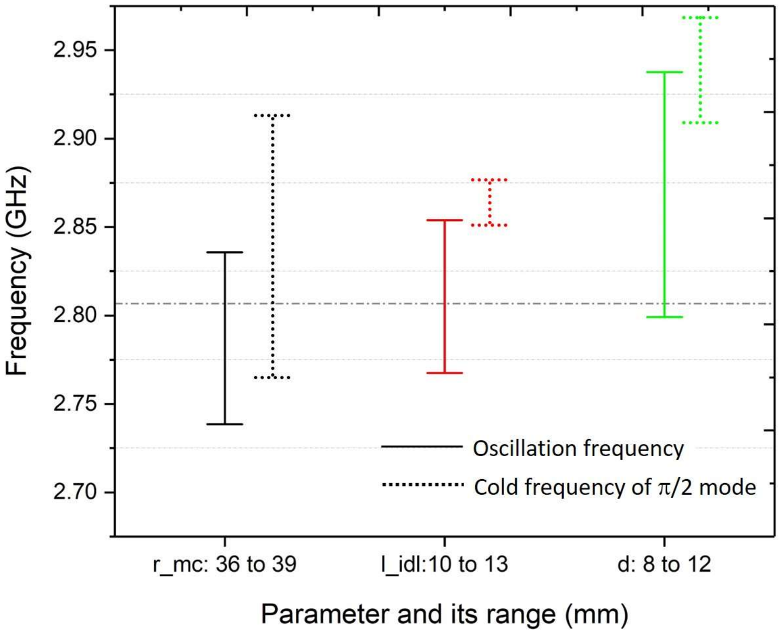

Figure 4.6: Frequency tunability achievable by varying the dimensional parameters of modulation section.

The r_mc and l_idl are easily alterable, even during the repetitive pulse operation. Coupling depth d causes maximum change in oscillation frequency. However, it is difficult to vary the coupling depth d in real time. In all the cases, the oscillation frequency has been found to be less than the corresponding cold frequency of $\pi/2$ mode, showing evidence of beam loading.

4.4.5 Phase-space plot

A phase space plot shows the variation of velocity, normalized momentum, energy, or Lorentz factor of all particles as a function of spatial coordinate in all possible combinations along the two axes. Phase space monitors are set at the beginning of the simulation to record the normalized momentum, and energy of electrons along the axial direction. Initially the phase space were recorded covering the entire simulation time by setting a larger time interval. Later, the start-stop time and interval was precisely adjusted to have detailed observations of different stage of the RF oscillation. Figure 4.7 shows the particle preview of normalized momentum in real space at an arbitrary time, after the oscillation has build up. Figure 4.8 shows the phase space of electron's energy during the initial stage of oscillation. Three frames are combined in each of the half cycles to have a clear view of electron's energy with time. Figure 4.9, and 4.10 show the electrons energy during a complete cycle of RF oscillation. These can be understood with the help of Figure 4.8, and Figure 4.11.

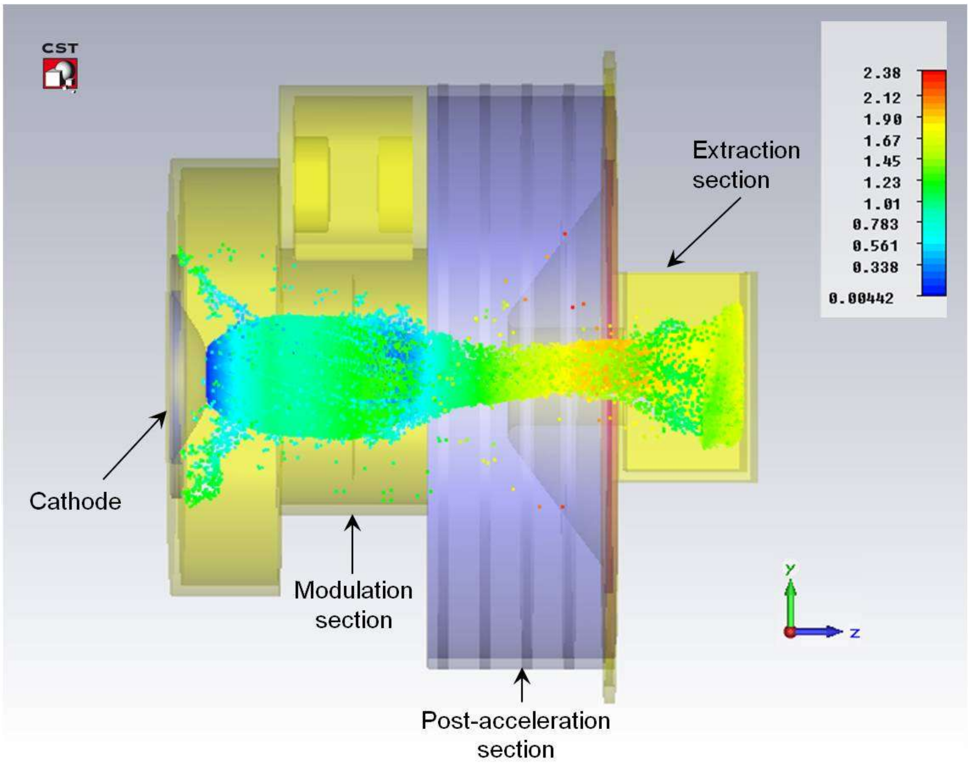

Figure 4.7: Electron positions in real space. Color-bar shows the normalized momentum.

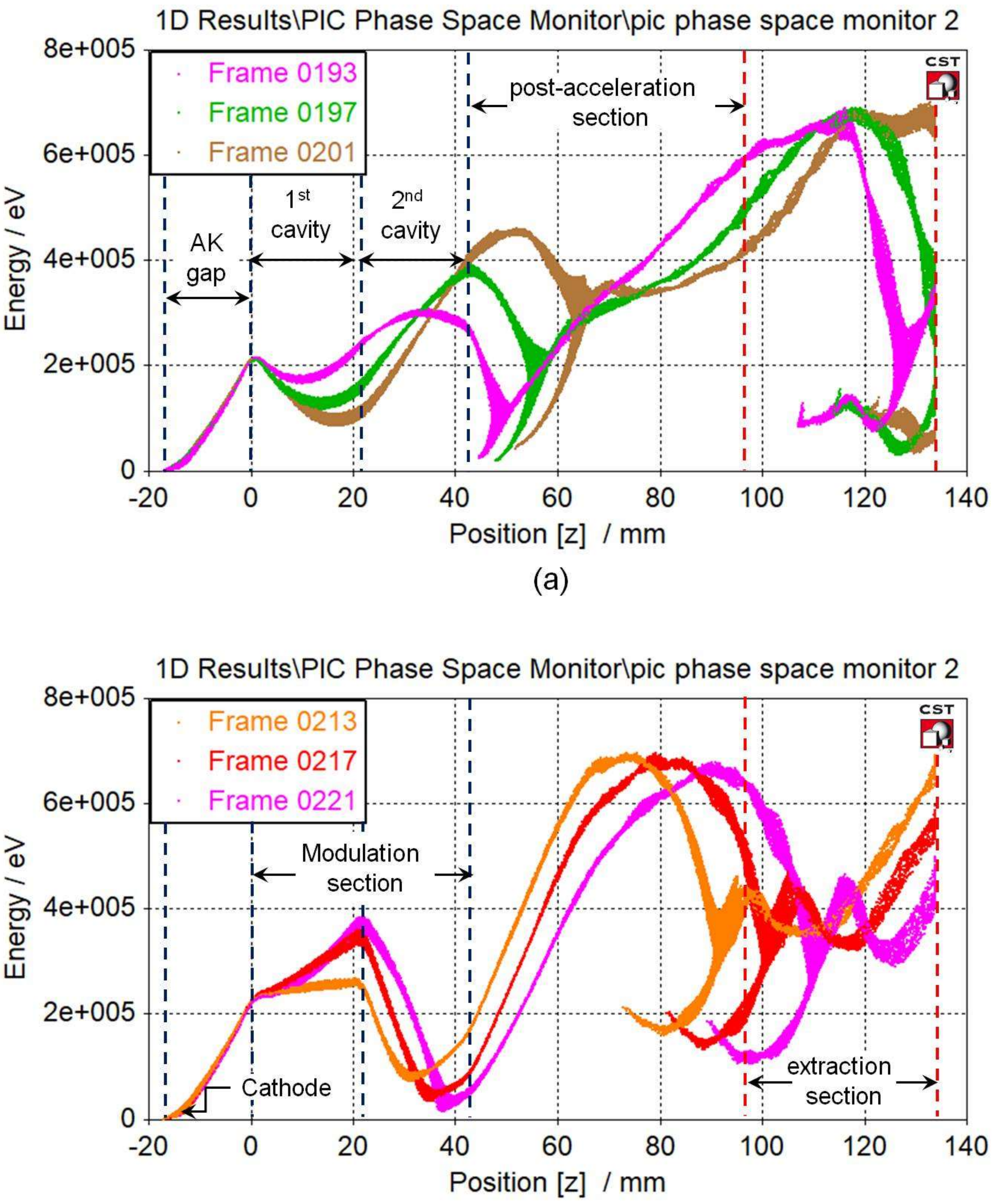

(a)

(b)

Figure 4.8: Phase space plot of electron energy (eV). Three combined frames showing (a) deceleration in the first cavity and acceleration in the second, (b) acceleration in the first cavity and deceleration in the second.

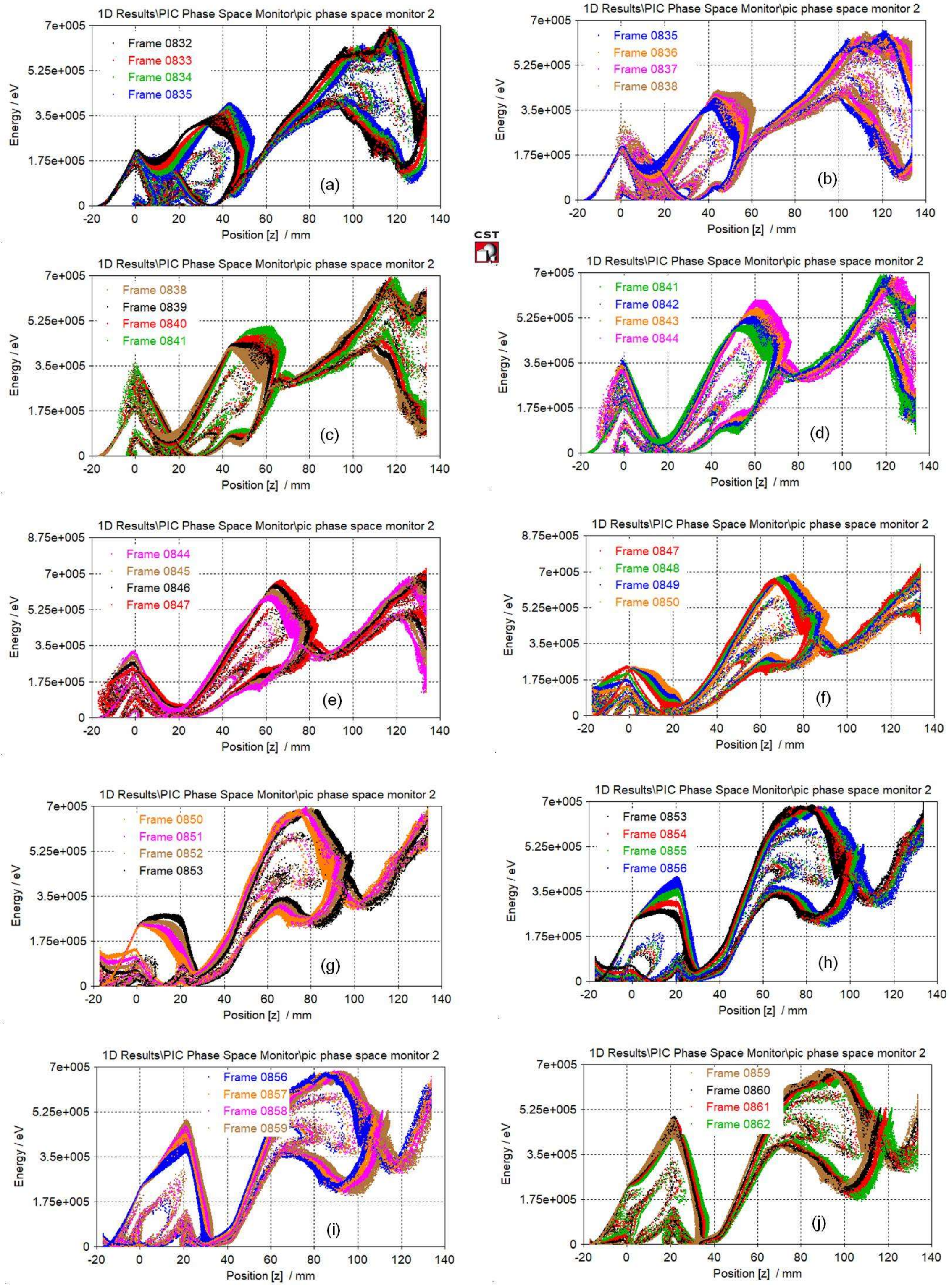

Figure 4.9: Phase space plot showing energy of electrons (eV) during a complete cycle of oscillation (part 1 of 2).

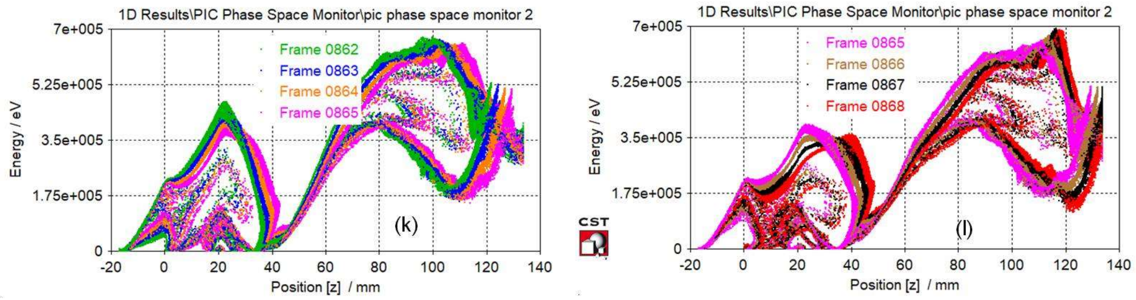

Figure 4.10: Phase space plot showing energy of electrons (eV) during a complete cycle of oscillation (part 2 of 2).

Figure 4.11 (a) and (b) show the electron's normalized momentum during two opposite cycles of RF oscillation. In simulation, the modulation section has been kept at ground potential, whereas the cathode and the post acceleration sections were supplied with -200 kV and 400 kV, respectively. So, the electrons covered the AK gap with a constant velocity, in both the half cycles and their normalized momentum became 1 (energy reached 200 keV in Figure 4.8) before they entered the modulation section. Here beam field interaction takes place in all three normal modes, but the $\pi/2$ mode grows in amplitude. In one-half cycle of this mode, the energy get decreased in first and increased in the second cavity (Figure 4.8 (a)). In the other half cycle, the opposite take place (Figure 4.8 (b)). This eventually segregates the beam into dense electron bunches. This bunch again gains momentum in the post-acceleration region and finally reaches normalized value 2, as the applied post-acceleration voltage is twice the anode-cathode voltage, which results in a reduction in energy spread shown in Figure 4.12 (a). The reduction in velocity spread, at the same instant of time, can be visualized more clearly from Figure 4.12 (b). The bunch then losses kinetic energy in the extraction section making the output electric field amplitude go from minima to maxima. A sequence of opposite phenomena occur in the modulation, and the extraction section during the other half cycle of the oscillation as shown in Figure 4.11(b).

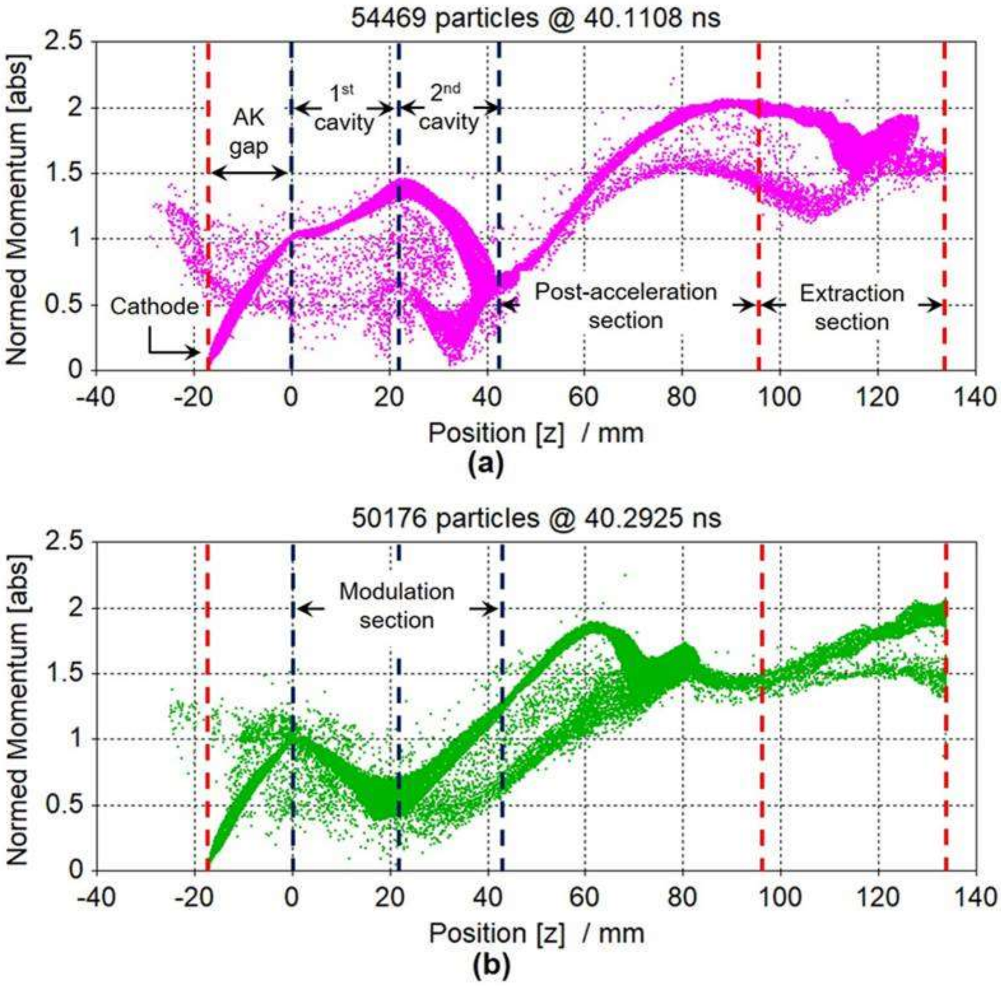

Figure 4.11: Phase space plot showing normalized momentum vs position at an instant of (a) first and (b) second half cycle of RF oscillation. The dotted lines indicate different sections.

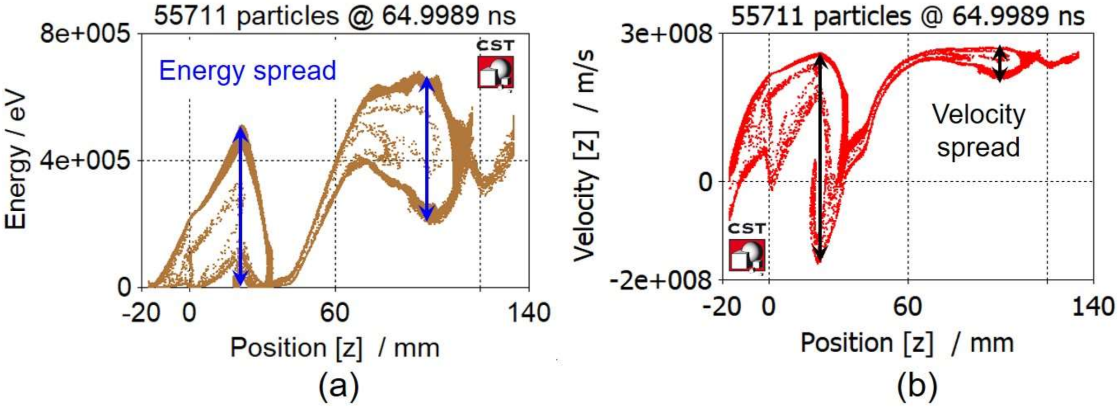

Figure 4.12: Reduction in (a) energy spread, and (b) velocity spread in the post acceleration section, with respect to the modulation section,respectively.

4.4.6 Effect of Idler disc length (l_{idl}) and Coupling depth (d) on the device performance

The change in idler disc length (l_idl) primarily results in change in mode separation. PIC simulation predicts better output power, and efficiency when the mode separation increases. Figure 4.13 shows the output power with increasing idler disc lengths, that causes higher separation among the three cavity modes. The efficiency is calculated using

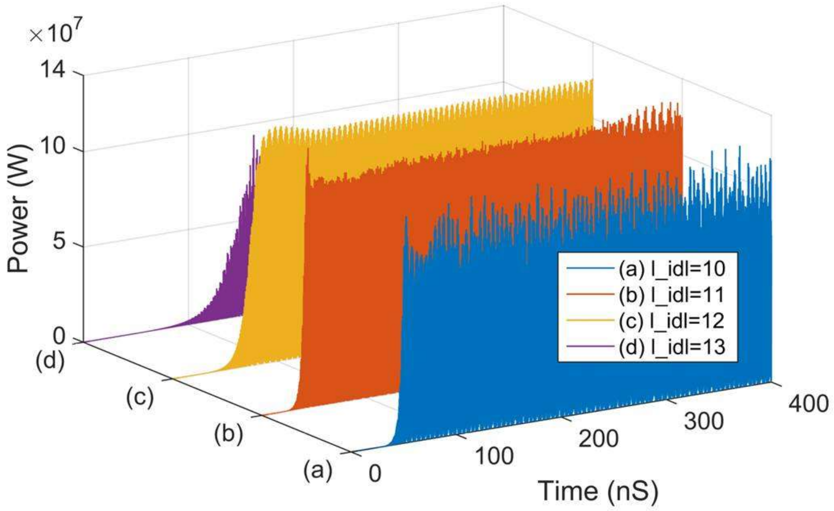

Figure 4.13: Output power (W) at different idler disc lengths (mm).

$$\eta = \frac{P_{out}}{(CAT\_V + PA\_V) \times I} \times 100\%, \tag{4.1}$$

where CAT_V and PA_V are the cathode and post-acceleration voltage (Volt), and I is the collector current (A). Output power and efficiency are tabulated for different l_idl in Table 4.2. The spectrum of the time signal is obtained by taking FT of the port signal in post-processing and shown in Figure 4.14. It was noticed that the beam dump does not cause any significant change in result in the present simulation setup, but it increases the computational resources as well as the simulation time required, hence it is not modeled.

The increase in coupling depth resulted in frequency tuning and a significant increase in efficiency. An initial increase in d resulted in gradually increasing efficiency up to a

Table 4.2: Frequency, Output power and efficiency at different idler disc length

l_idl (mm)	Oscillation frequency (GHz)	Output power (MW)	Efficiency (%)
10	2.876	111	34
11	2.805	120	37
12	2.790	117	33
13	2.796	87	24

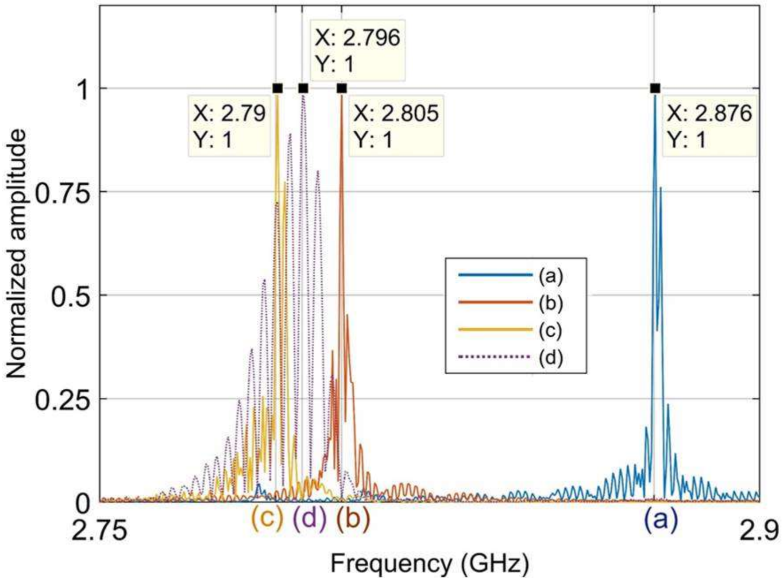

Figure 4.14: Fourier transform of output port signals for l_idl = (a) 10 mm, (b) 11 mm, (c) 12 mm, and (d) 13 mm.

certain limit. Further increase in d did not improve efficiency. Instead, the efficiency got reduced as the peak axial electric field shifted away from the beam axis, modifying the beam trajectory. This also increases the beam interception by different parts of the tube. The frequencies and the corresponding efficiencies are listed in Table 4.3.

4.5 Conclusion

The following conclusions are made from the PIC simulation results–

The obtained output frequency from PIC solver is found to be closest to the $\pi/2$ mode

Table 4.3: Summary of frequency and efficiency at different coupling depth

Coupling depth d (mm)	Oscillation frequency (GHz)	Efficiency (%)
8	2.9404	20.94
9	2.9351	21.64
10	2.8517	35.40
11	2.8067	37.15
12	2.8077	34.42

cold test frequency predicted by Eigenmode solver, which confirms only $\pi/2$ mode transfers a net energy from the beam to the field.

The reduction in the output frequency compared to the cold frequency reveals the effect of beam loading. FT of the output signal is relatively monotonous in comparison to VIRCATOR and RM as the interaction with 0, and π modes do not play any role in beam bunching. Unwanted mode jumping as well as frequency chirping were not found. However, pulse shortening may occur due to an enhanced electric field inside the cavity.

Increasing the mode separation (by tuning the idler disc) shows improvement in the output power and efficiency up to a critical level accompanied by a down-shift in frequency, resulting from the declining $\pi/2$ mode. An increase beyond this point cuts down both the output power and efficiency. When mode separation is further increased, the pulse duration is reduced substantially, reducing in energy per pulse. The oscillation frequency increases in this case than that of the highest efficiency case. The output signal spectrum shows the power is being distributed among the higher and lower spectral components (Figure 4.14 (d)), reducing the purity of the oscillation.

The effect of coupling depth d on the device performance has also been studied (Table 4.3).

The phase-space plot provides important insight into the device operation, and it also shows the decrease in kinetic spread due to the application of post-acceleration voltage. The reduction in energy spread with the application of post acceleration potential has been discussed using the phase space plot.

The range of frequency tunability achievable through tuning the cavity parameters has also been demonstrated.